Electronic Supplementary Material (ESI) for Journal of Materials Chemistry A. This journal is © The Royal Society of Chemistry 2025

Electronic Supplementary Information

for

Morphology and electron regulation of B-WS_2@MXene nanosheets array heterojunction to upgrade capacity and longevity of lithium-sulfur batteries

Jiayu Huang,[a] Dan Wang,*[,a,c] Zhibin Cheng,[b] Xiaofei Xie,[a] Bowen Chang,[a] Xiaoju Li,*[,a,b] Ruihu Wang*[,a,c]

[a]*Hebei Key Laboratory of Functional Polymer, School of Chemical Engineering and Technology, Hebei University of Technology, Tianjin 300130, China*

[b] *Fujian Key Laboratory of Polymer Materials, College of Chemistry and Materials Science, Fujian Normal University, Fuzhou 350007, China*

[c] *State Key Laboratory of Structural Chemistry, Fujian Institute of Research on the Structure of Matter, Chinese Academy of Sciences, Fuzhou, Fujian 350002, China*

*Corresponding authors.

E-mail addresses: xiaoju@hebut.edu.cn, 2022921@hebut.edu.cn, ruihu@fjirsm.ac.cn

Materials

Thioacetamide, WCl_6, Na_2BO_2, Ti_3AlC_2, Sulfur and LiF were purchased from Shanghai Adamas-beta Reagent Co. Carboxylate-functionalized multiwalled carbon nanotube (CNT, >99.9%) was purchased from Aladdin Industrial Corporation (Shanghai, China). Lithium sulfide was purchased from Alfa Aesar. All chemicals were commercially available and used without further purification.

Structure Characterizations

Powder X-ray diffraction (XRD) patterns were recorded in the range of $2\theta = 5\text{-}70°$ on a desktop X-ray diffractometer (Bruker D8 Discover) with Cu Kα radiation. Elemental analysis was performed using an Elementar Vario MICRO Elemental analyzer. Scanning electron microscope (SEM) images were obtained with a TESCAN MIRA LMS field-emission scan electron microscope. Transmission electron microscope (TEM) images were obtained on TF20. Thermogravimetric analysis (TGA) was measured at a heating rate of 10 °C min^{-1} using a STA449 F5 Jupiter XXXhermos gravimetric analyzer (NETZSCH). Nitrogen adsorption-desorption isotherms were measured at 77 K with a JW-BK200C gas adsorption analyser after the sample was first degassed at 120 °C under vacuum for 12 h prior to the measurement. The specific surface area was calculated using the Brunauer-Emmett-Teller (BET) equation, and the total pore volumes were calculated from the amount adsorbed at a relative pressure (P/P_0) of 0.99. The mesopore size distribution was obtained based on BJH analysis of the adsorption branches of the isotherms. X-ray photoelectron spectroscopy (XPS) measurements were performed on a Thermo Scientific K-Alpha spectrometer using nonmonochromatic Al Kα X-ray as the excitation source and C 1s (284.8 eV) as the reference line. Electron paramagnetic resonance spectroscopy (EPR) was performed using a Bruker EMX PLUS machine. The magnetic field was set to 2000-5000 G and the sweep speed is 10 G s^{-1}.

Preparation of B-WS_2@MXene-PP separator

The separator was obtained by typical vacuum filtration method. After B-WS_2@MXene and polyvinylidene difluoride (PVDF) was mixed in a weight ratio of 9:1 in DMF (50 mL) under sonication for 2 h, the mixture was filtered on commercial polypropylene separator (Celgard 2500) with the mass loading of 0.1 mg cm^{-2}. The resultant B-WS_2@MXene-PP separator was dried under vacuum at 40 °C for 48 h and cut into circular disks for direct use.

WS_2@MXene-PP and WS_2-PP separators were prepared through similar procedures except B-WS_2@MXene was replaced by WS_2@MXene and WS_2, respectively.

Preparation of CNT/S

The CNT/S composite was prepared using conventional melt-diffusion method. In a typical procedure, the mixture of CNT and sulfur with appropriate mass ratio was ground and dispersed in CS_2 solution, the mixture was stirred at room temperature until CS_2 was completely evaporated. The resultant mixture was heated at 155 °C for 24 h. The product was collected after cooling to room temperature to generate the CNT/S composite. The sulfur contents were determined by TGA measurements.

Preparation of regular cathodes

80 wt% active materials (CNT/S), 10 wt% conductive agent and 10 wt% PVDF were mixed with 1-methyl-2-pyrrolidinone (NMP) to form a homogeneous slurry. The slurry was pasted onto aluminum foil and dried at 60 °C for 24 h, subsequent pressing with a roller machine and cutting into circular pieces generated the test electrodes.

Adsorption test of lithium polysulfides.

All samples were dried under vacuum at 60 ºC overnight before the adsorption test. Li_2S_6 was prepared by chemical reaction of sulfur and an appropriate amount of Li_2S in 1,3-dioxolane and dimethoxymethane (DOL/DME 1:1 by volume). The solution was stirred under nitrogen atmosphere at 60 ºC for 48 h to produce a brownish red Li_2S_6 stock solution (0.2 M). The Li_2S_6

solution was then diluted to 20 mM, and 15 mg of sample was added into diluted solution (2 mL) for the polysulfide adsorption test.

Electrochemical Characterization.

Electrochemical experiments were performed via CR2025 coin-type cells assembled with lithium metal as the counter and reference electrode in an argon-filled glovebox, where the moisture and oxygen levels were both kept below 1.0 ppm. The modified separators were used as the separator. The electrolyte was 1 M lithium bis(trifluoromethane) sulfonimide with 1% anhydrous $LiNO_3$ dissolved in DOL/DME (1:1 by volume). The electrolyte/sulfur ratio was 15 μL (electrolyte) /mg (sulfur). The discharge/charge measurements were conducted at a voltage interval from 1.5 to 3.0 V using a Neware battery test system (Neware Technology Co.). Before testing, the cells were aged for 24 h. Cyclic voltammetry (CV) and electrochemical impedance spectroscopy (EIS) measurements were performed on GAMRY INTERFACE 1010 electrochemical workstation. The CV scan rate was fixed at 0.1 mV s^{-1} and EIS was measured with an applied sinusoidal excitation voltage of 5 mV in the frequency range from 100 kHz to 0.1 Hz.

Symmetrical cell assembly and measurements.

The electrodes for symmetrical cells were fabricated in the absence of sulfur according to the modified literature method. Typically, each electrode material (B-WS_2@MXene, WS_2@MXene and WS_2) and PVDF binder with a mass ratio of 9:1 were dispersed in NMP. The resultant slurry was coated on carbon fiber paper using a blade. The electrode disks with a diameter of 14.0 mm were punched after thorough drying. These disks were used as the identical working and counter electrodes. The mass loading of active material was ~1.0 mg cm^2. The mixture of Li_2S_6 (0.5 mol L^{-1}) and LiTFSI (1 mol L^{-1}) in DOL/DME (50 μL, 1:1 by volume) was used as the electrolyte. The CV measurement of the symmetric cell was conducted at a scan rate of 5 mV s^{-1} with a voltage window between -1 and 1 V. The electrochemical impedance spectroscopy (EIS) measurement was performed at open-circuit voltage with a sinusoidal voltage of amplitude of 10 mV and a frequency range from 10^6 to 0.01 Hz.

Nucleation test of Li_2S.

The Li_2S_8 stock solution was prepared by combining sulfur and Li_2S powder at a molar ratio of 7:1 in tetraglyme under vigorous stirring for 24 h, which was used as the catholyte. The electrode material (WS_2, WS_2@MXene and B-WS_2@MXene) and PVDF binder with a mass ratio of 9:1 were dispersed in NMP. The resultant slurry was coated on carbon fiber paper using a blade. The electrode disks with a diameter of 14.0 mm were punched after thorough drying. These disks were used as the identical working and lithium metal as the counter electrodes. The mass loading of active material was ~1.0 mg cm^2. 20 μL of Li_2S_8 catholyte was dropped on the side of WS_2, WS_2@MXene or B-WS_2@MXene working electrode, while 20 μL electrolyte without Li_2S_8 was added to the side of counter electrode. The assembled cells were discharged galvanostatically to 2.06 V at 112 μA and then discharged potentiostatically to 2.05 V for Li_2S nucleation/growth. The cells were disassembled after 18000s discharge for structural and morphological characterizations.

Dissolution test of Li_2S.

The cells of the dissolution test are exactly the same as that of the nucleation test. The assembled cells were first galvanostatically discharged to 1.80 V at 0.10 mA, and subsequently galvanostatically discharged to 1.80 V at 0.01 mA for complete transform of Li_2S_8 to solid Li_2S. Then the cells were potentiostatically charged at 2.40 V for the oxidization of Li_2S into soluble polysulfides.

The electrochemically active surface area (ECSA).

The electrode material (WS_2, WS_2@MXene and B-WS_2@MXene) and PVDF binder with a mass ratio of 9:1 was dispersed in NMP with stirring. The resultant slurry was coated on carbon fiber paper. The punched electrode disks (14.0 mm) were used as working and counter electrodes. 0.5 mol L^{-1} Li_2S_6 and 1 mol L^{-1} LiTFSI in 40 μL DOL/DME (1:1 by volume) were used as the electrolyte. CV measurements of the symmetrical cells were performed in the voltage window of from 2.6 to 3 V at scan rate of 10-100 mV s^{-1}, respectively. C_{dl} values of all the material were calculated from multiple CV scan with different scan rates (ν) within a narrow potential window.

The calculation for diffusion coefficient of Li ions.

The diffusion coefficient of Li ions can be described by the Randles-Sevcik equation:

$$I_P = (2.69 \times 10^5) n^{1.5} S D^{0.5} C v^{0.5} \quad (1)$$

where I_P is the peak current, n is the electron charge number (n = 2), S is the area of the electrode (1.54 cm^2), D is the diffusion coefficient of the Li ions, C is the Li-ion concentration change during reaction (0.001 mol cm^{-3}), and v is the scan rate. Because n, S and C are given data, there is a linear relationship between I_p and $v^{0.5}$, and D is correlated positively to the slopes of the curves (I_p / $v^{0.5}$).

Electronic Conductivity Test.

The electronic conductivity of WS_2, WS_2@MXene, and B-WS_2@MXene was evaluated by means of a constant voltage polarization test. An electrochemical workstation was employed to subject the pressed material to direct current polarization at a constant voltage for a specified period of time. This procedure enabled the generation of a current-time curve, which was then utilized to calculate the electronic conductivity at steady state current. The calculation equation:

$$R_{e-} = U/I \quad (2)$$

$$\sigma_{e-} = L/(R_{e-} \times S) \quad (3)$$

where R_{e-} is the electronic resistance (Ω) of WS_2, WS_2@MXene and B-WS_2@MXene slices, U is the constant voltage of the test setup (10 mV), I is the steady-state current value for 1000 s of direct current polarization (mA), $\sigma_{e-}$is the electronic conductivity of the three materials (mS cm^{-1}), L is the thickness of the material to be pressed (cm), S is the area of the blocking electrode (cm^{-2}).

Ionic Conductivity Test.

The ionic conductivity of the modified separators (WS_2-PP, WS_2@MXene-PP, B-WS_2@MXene-PP) were calculated by the EIS method. In a coin cell, each diaphragm saturated with electrolyte is sandwiched between two stainless steel electrodes whose ionic conductivity is obtained according to the following equation:

$$\sigma_{Li}{}^{+}= L/(R_b \times S) \quad (4)$$

where σ_{Li+}, L, A, and R_b denote ionic conductivity (mS cm^{-1}), membrane thickness (cm), stainless steel electrode area (cm^{-2}), and resistance (Ω), respectively.

Lithium-Ion Mobility Test.

The lithium-ion migration ($t_{Li}{}^{+}$) of the modified separators (WS_2-PP, WS_2@MXene-PP, B-WS_2@MXene-PP) were determined by the timed current method at a constant step potential of 10 mV. In a coin cell (CR 2032), each separator is sandwiched between two lithium metal electrodes, and the lithium ion migration number is calculated from the ratio of the steady state current to the initial state current according to the following equation:

$$t_{Li}{}^{+}=I_{ss}\ (\Delta V-I_0R_0)/I_0(\Delta V-I_{ss}R_{ss}) \quad (5)$$

where $t_{Li}{}^{+}$, I_{ss} and I_0 denote the Li-ion migration number, steady state and initial state currents, respectively.

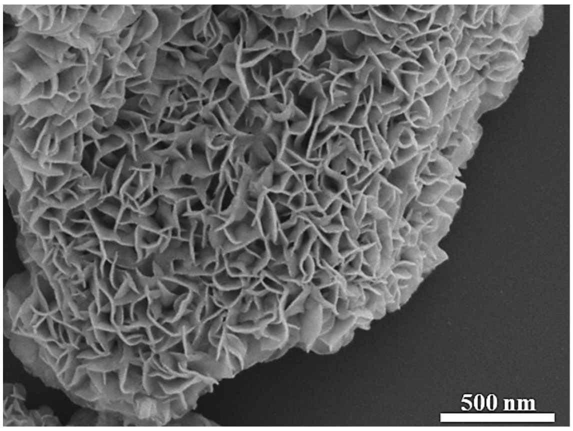

Fig. S1. SEM image for WS_2@MXene

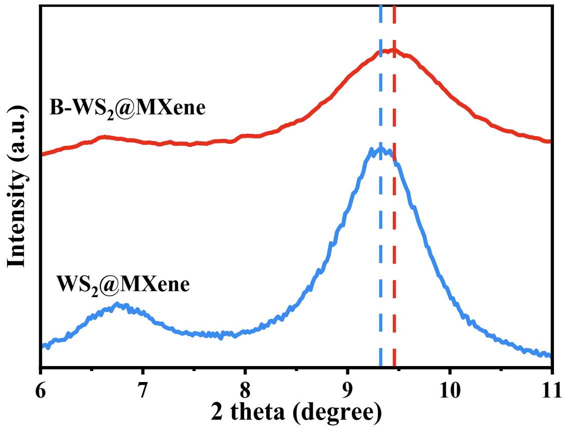

Fig. S2. XRD patterns in the range of 2θ = 6-11° for WS_2@MXene and B-WS_2@MXene.

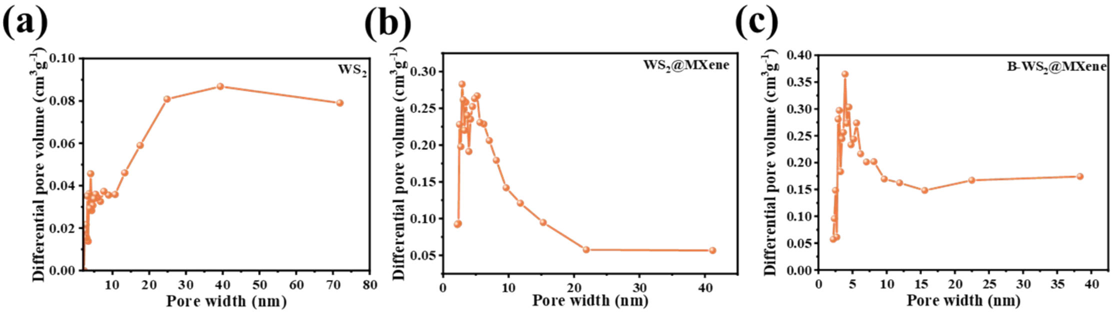

Fig. S3. Pore size distributions of (a)WS_2, (b) WS_2@MXene and (c) B-WS_2@MXene.

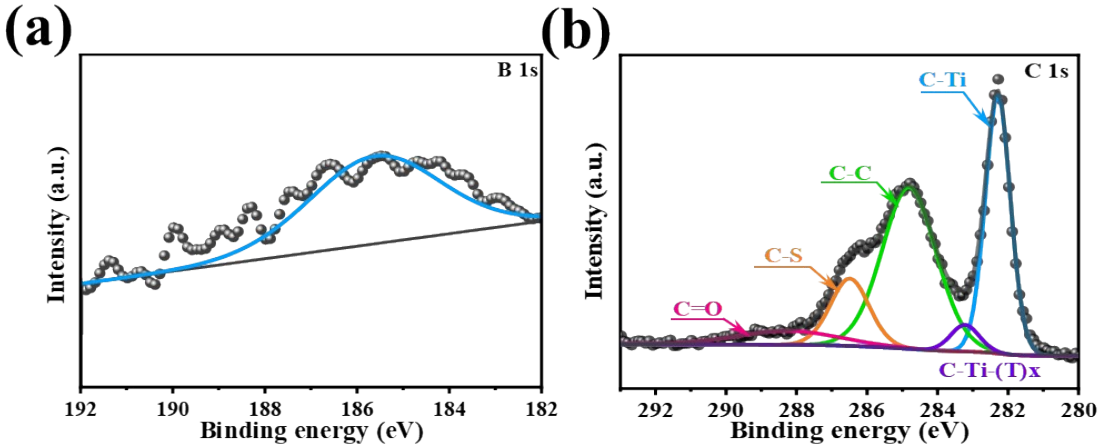

Fig. S4. (a) High-resolution B 1s XPS spectrum of B-WS_2@MXene. (b) High-resolution C 1s XPS spectrum of B-WS_2@MXene.

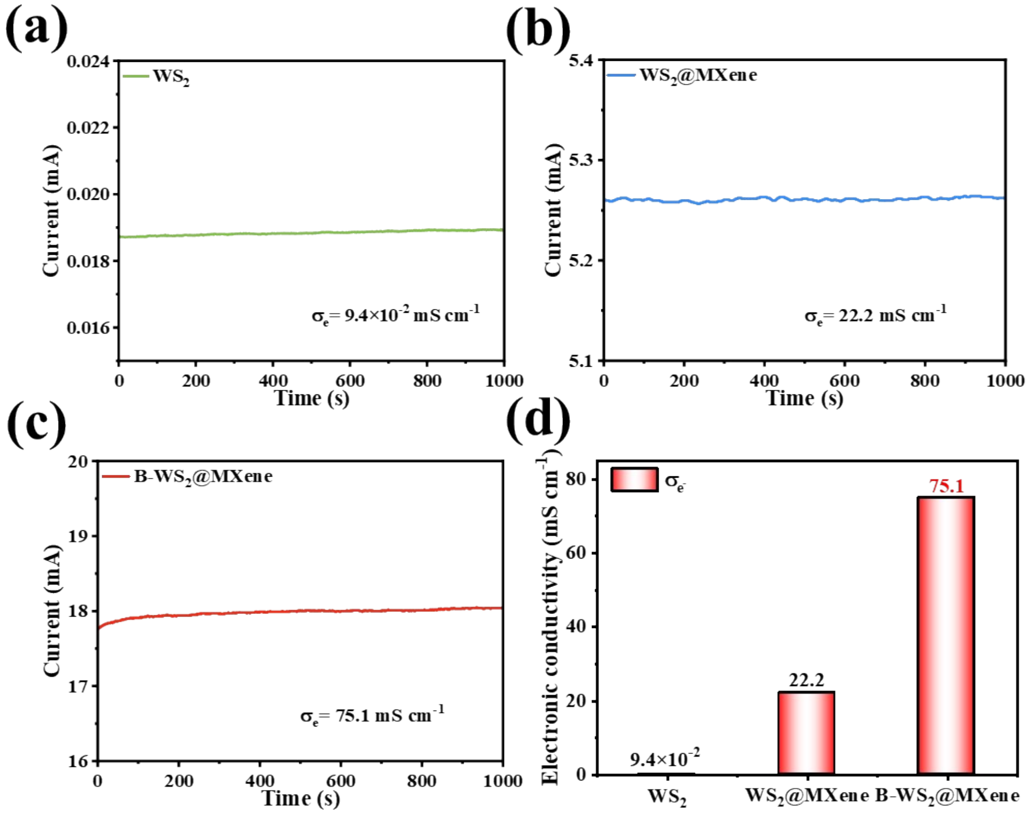

Fig. S5. (a-c) Time-current curves for (a) WS_2, (b) WS_2@MXene and (c) B-WS_2@MXene. (d) Comparison of electronic conductivity for WS_2, WS_2@MXene and B-WS_2@MXene.

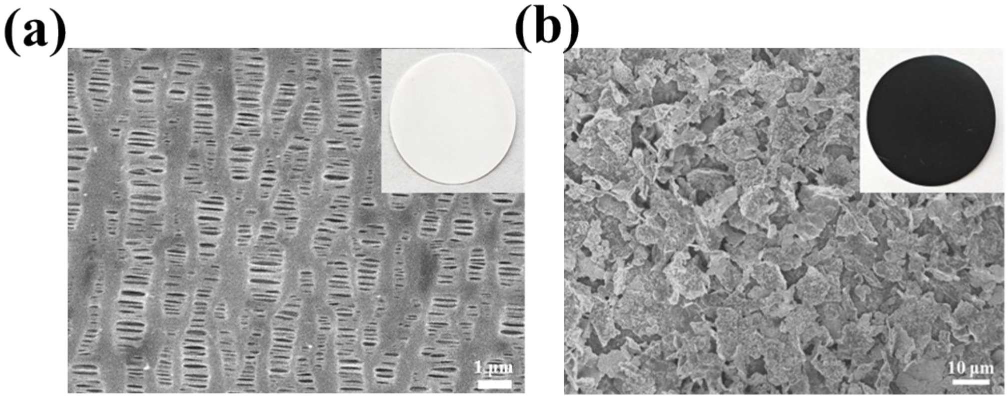

Fig. S6. SEM images and digital photographs (inset) for (a) PP and (b) B-WS_2@MXene-PP separators.

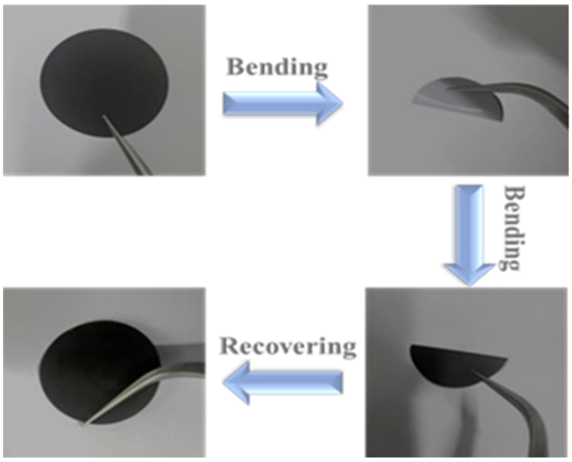

Fig. S7. The photographs for the B-WS_2@MXene-PP separator at bending state and after recovery.

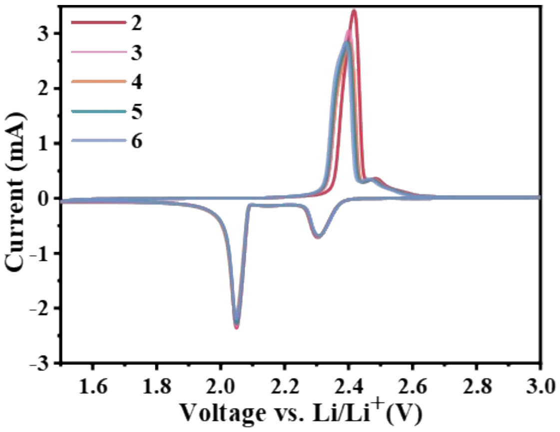

Fig. S8. CV profiles of B-WS_2@MXene-PP for consecutive six cycles.

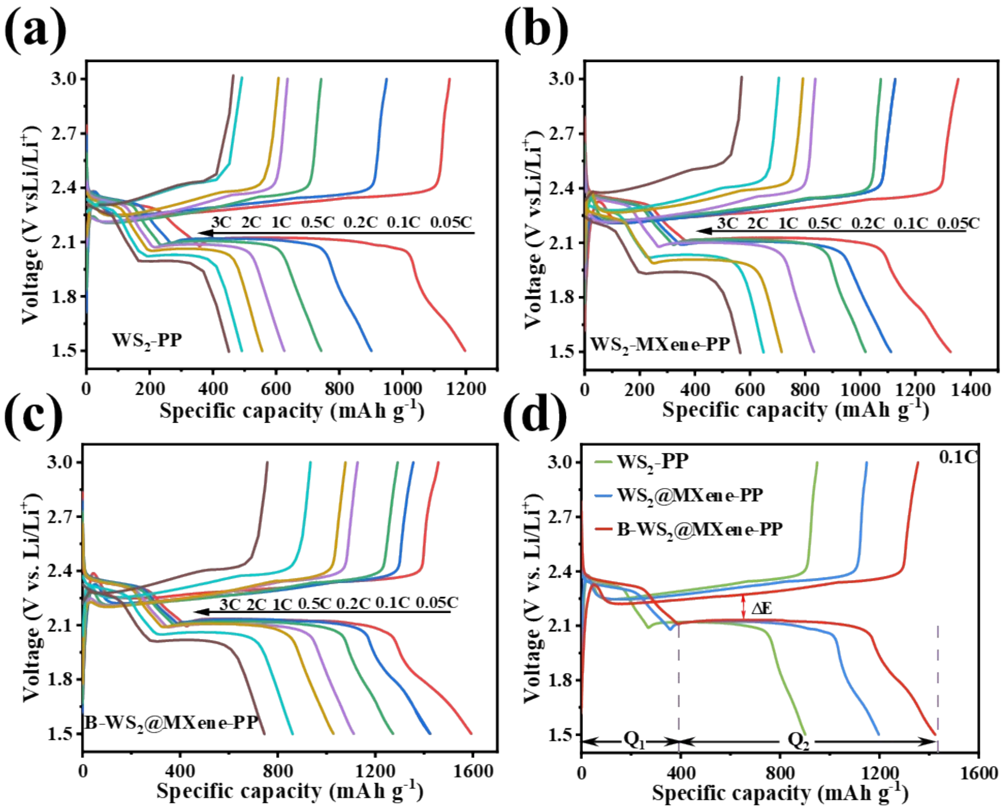

Fig. S9. Galvanostatic charge-discharge profiles at various rates for (a) WS_2-PP, (b) WS_2@MXene-PP and (c) B-WS_2@MXene-PP. (d) The galvanostatic charge/discharge curves.

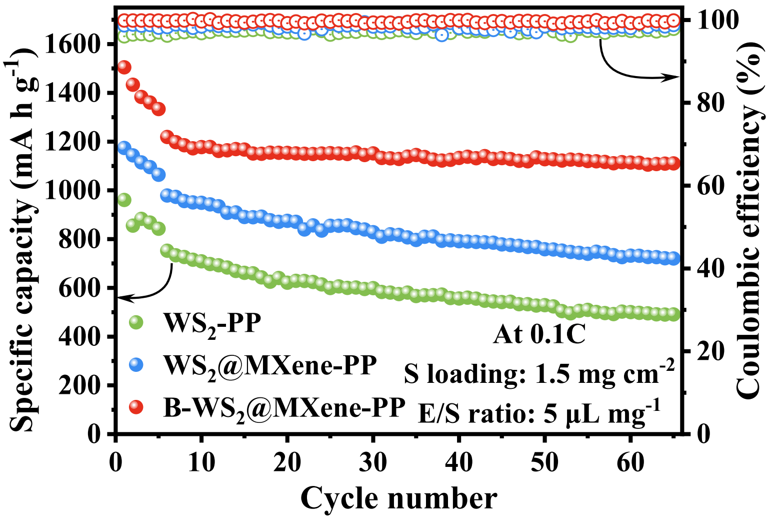

Fig.S10. Cycling stability for B-WS_2@MXene-PP, WS_2@MXene-PP and WS_2-PP at 0.1 C and low electrolyte/sulfur (E/S) ratios.

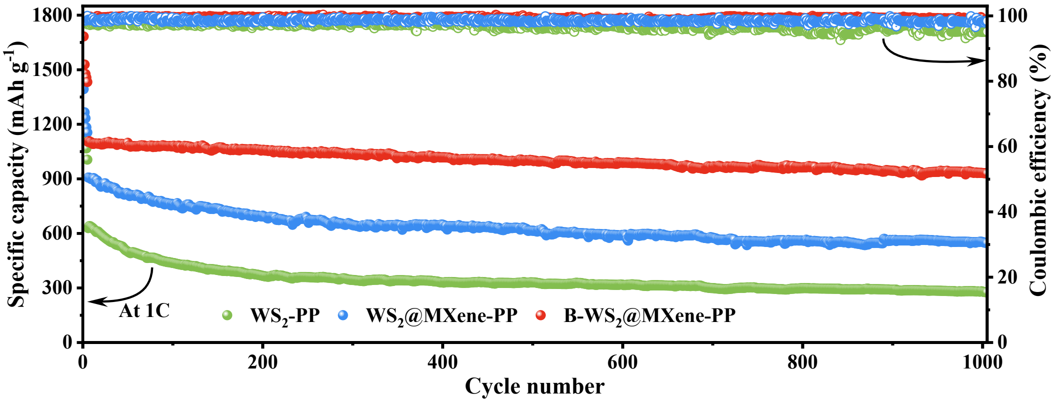

Fig. S11. Long-term cycling stability at 1 C for B-WS$_2$@MXene-PP, WS$_2$@MXene-PP and WS$_2$-PP.

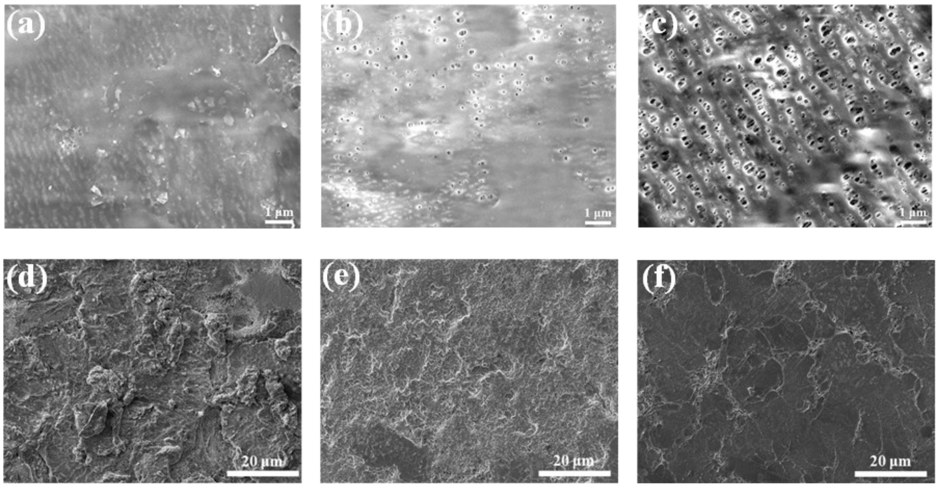

Fig. S12. SEM images for (a) post-WS$_2$-PP, (b) post-WS$_2$@MXene-PP and (c) post-B-WS$_2$@MXene-PP separators toward lithium anode after 200 cycles at 0.1 C. SEM images of lithium metal anode after 200 cycles at 0.1C for (d) WS$_2$-PP, (e) WS$_2$@MXene -PP and (f) B-WS$_2$@MXene-PP.

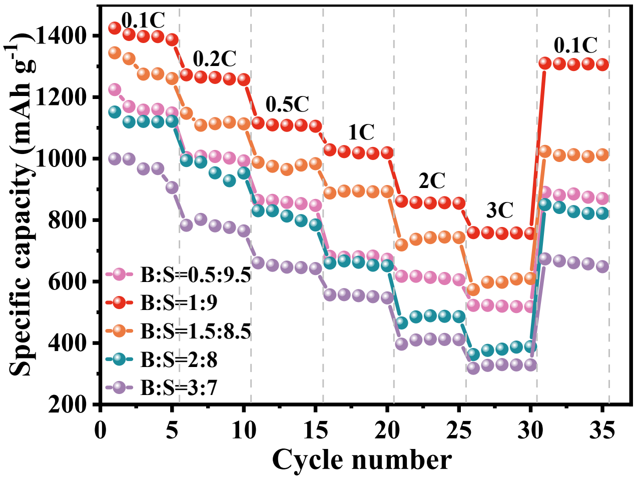

Fig. S13. The rate performance of B-WS$_2$@MXene-PP with different mass ratio of boron and sulfur sources for the synthesis of B-WS$_2$@MXene.

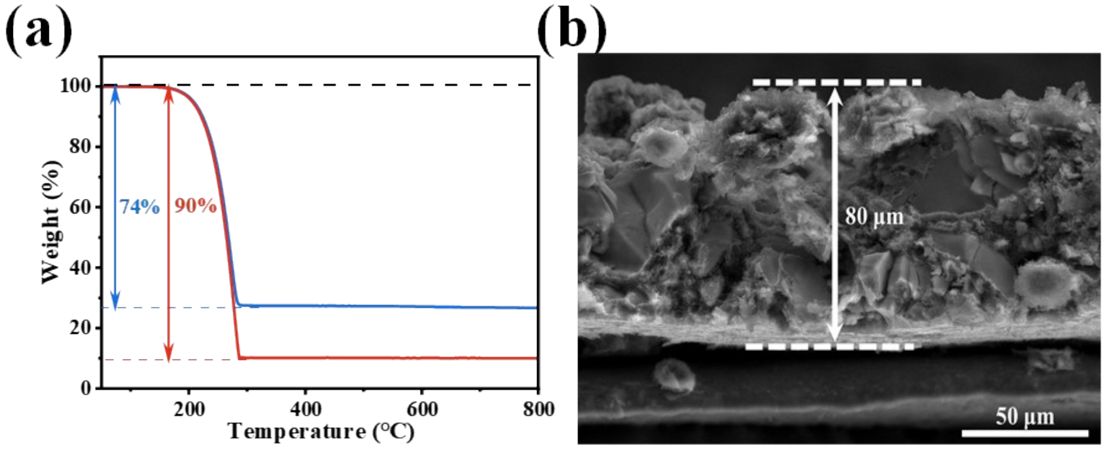

Fig. S14. (a) TGA curves of CNT-S composites with different sulfur contents. (b) Cross-sectional SEM image of CNT/S cathode with 90 wt% sulfur loading.

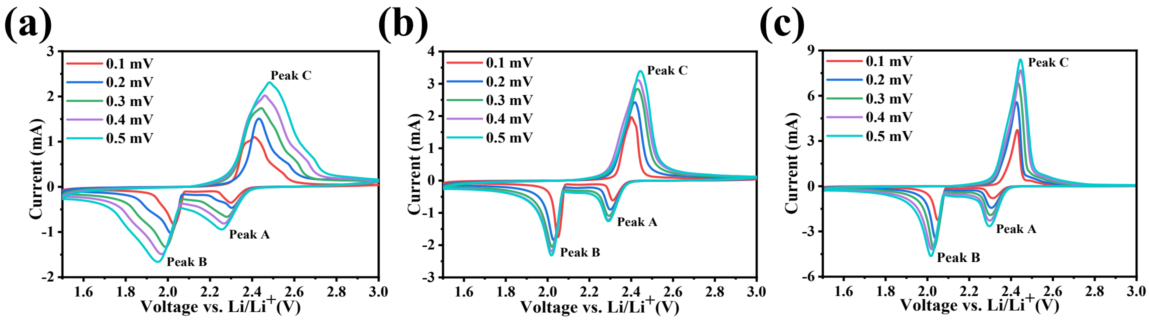

Fig. S15. CV curves of (a) WS_2-PP, (b) WS_2@MXene-PP and (c) B-WS_2@MXene-PP at different scan rates.

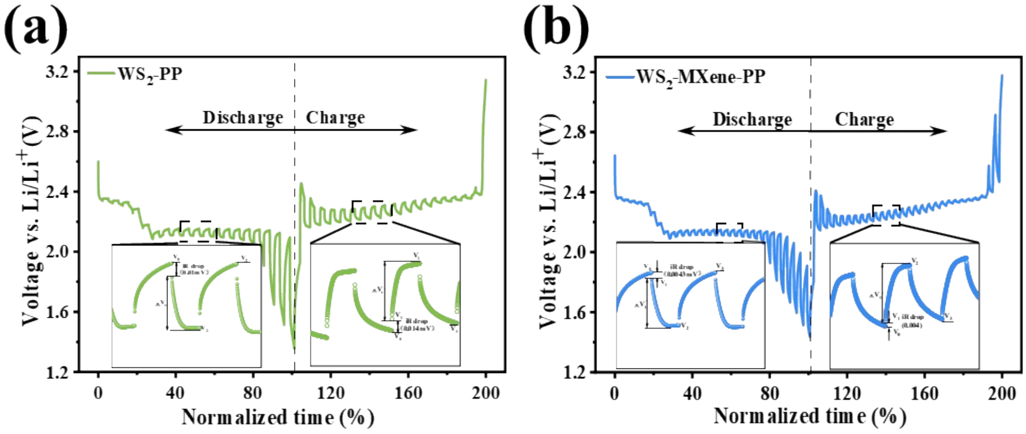

Fig. S16. GITT test curves of (a) WS_2-PP, (b) WS_2@MXene-PP.

The results of the GITT test allow for the calculation of the variation in internal resistance during charging and discharging.

$$iR_{drop}=V_0-V_1 \quad (6)$$

$$R_{internal}=|\Delta V|/I_{applied} \quad (7)$$

V_0 is the initial voltage of the pulse discharge, V_1 is the instantaneous voltage of constant current discharge, V_2 is the voltage at the end of constant current discharge, V_3 is the voltage after resting. The change in voltage is influenced by the internal ohmic impedance and charge transfer impedance of the cell, which is reflected in the iR drop. A higher level of ionic conductivity corresponds to smaller iR drop values. During the process of charging and discharging, $R_{internal}$ reacts to changes in resistance. The calculation of this reaction is done using the formula $\Delta V = V_1-V_2$, where Iapplied represents the applied current ($I_{applied}$ = 0.1 mA). The internal resistance value reflects the diffusion and charge transfer abilities of Li^+ during charging and discharging. $R_{internal}$ increases overall during discharging from S_8 to Li_2S and decreases overall during charging. This may be due to the continuous depletion of Li^+ and the decrease of active sites.

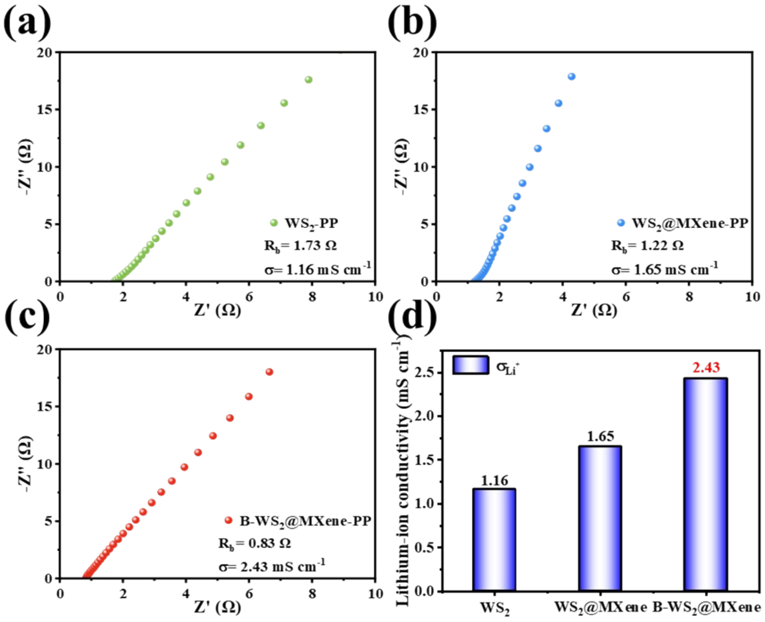

Fig. S17. (a-c) Li^+ conduction resistance and (d) Li^+ conductivity for WS_2-PP, WS_2@MXene-PP and B-WS_2@MXene-PP.

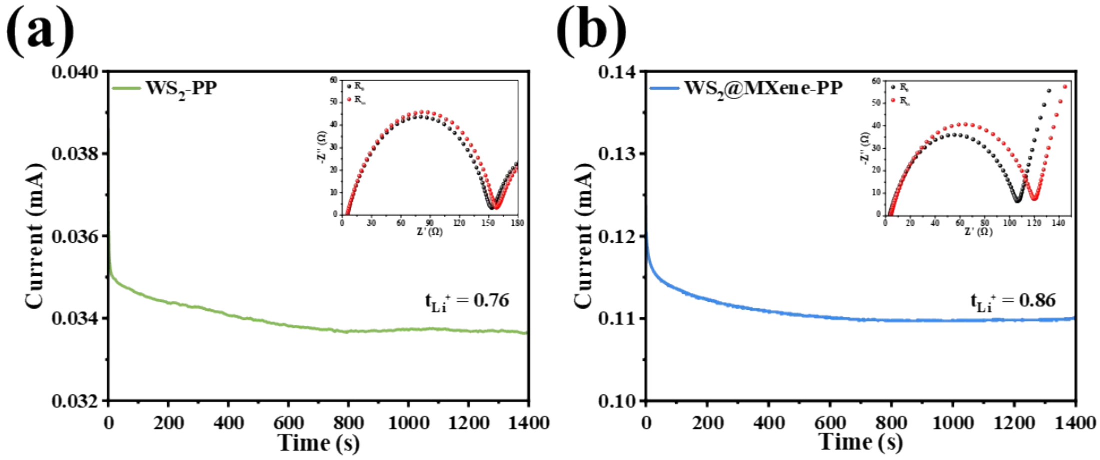

Fig. S18. I–t curves of the WS$_2$-PP and WS$_2$@MXene-PP.

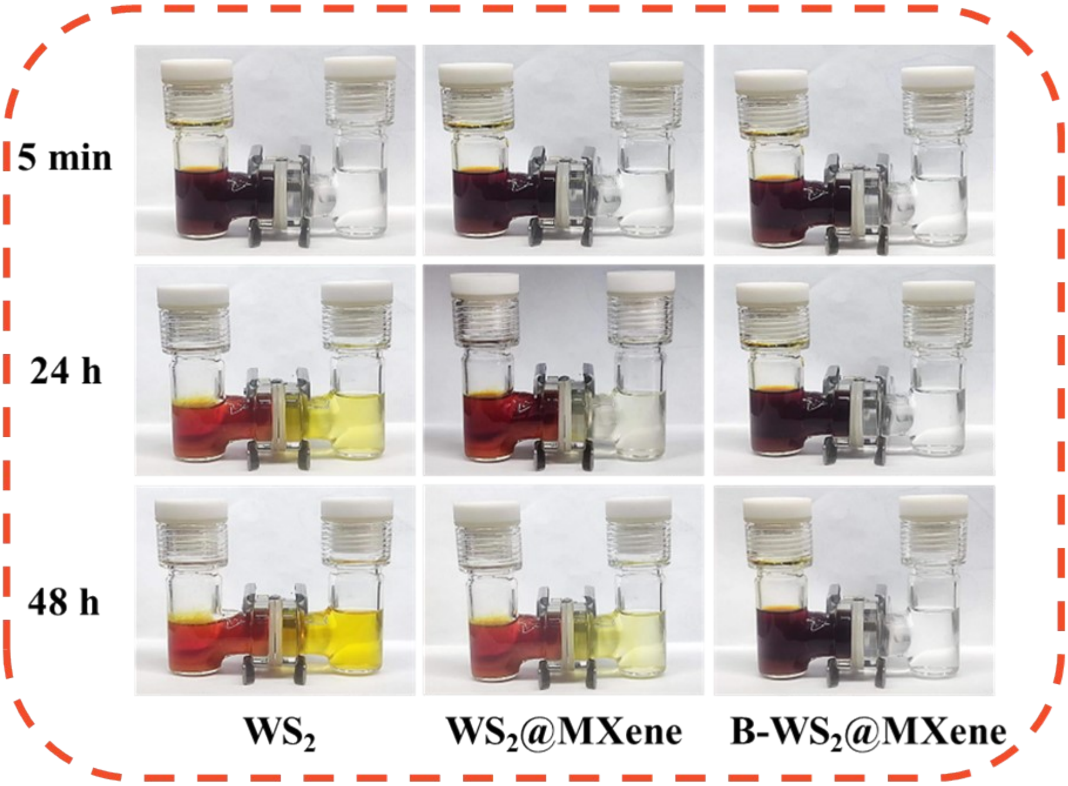

Fig. S19. Polysulfides permeation measurements for WS$_2$-PP, WS$_2$@MXene-PP and B-WS$_2$@MXene-PP separators.

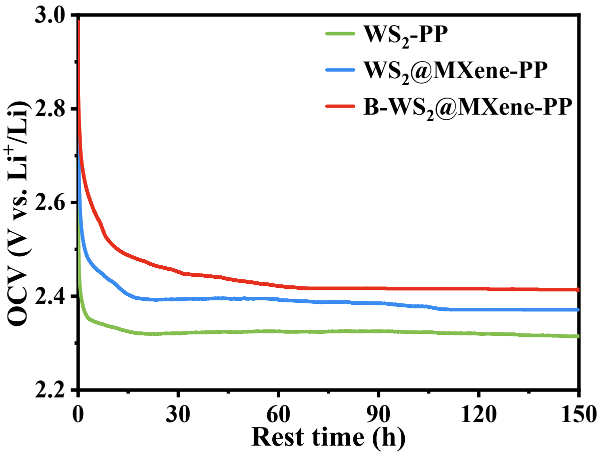

Fig. S20. Self-discharge behavior of WS$_2$-PP, WS$_2$@Mxene-PP and B-WS$_2$@Mxene-PP.

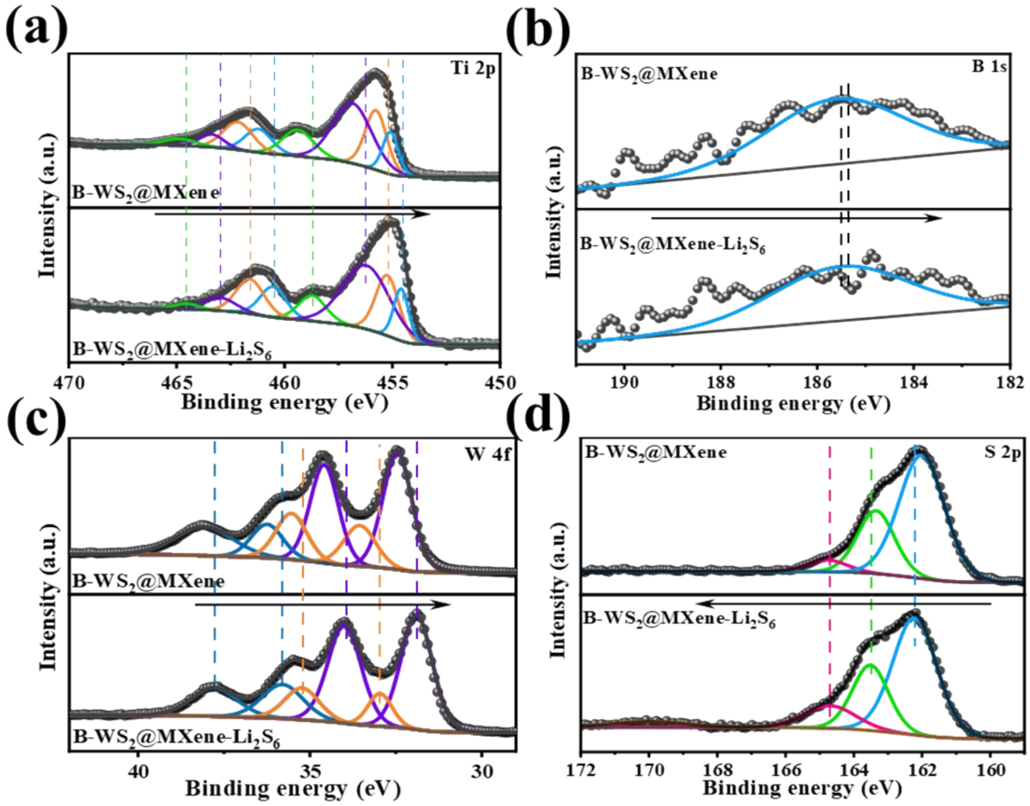

Fig. S21. (a) Ti 2p, (b) B 1s, (c) W 4f, and (d) S 2p of the B-WS$_2$@MXene-Li$_2$S$_6$.

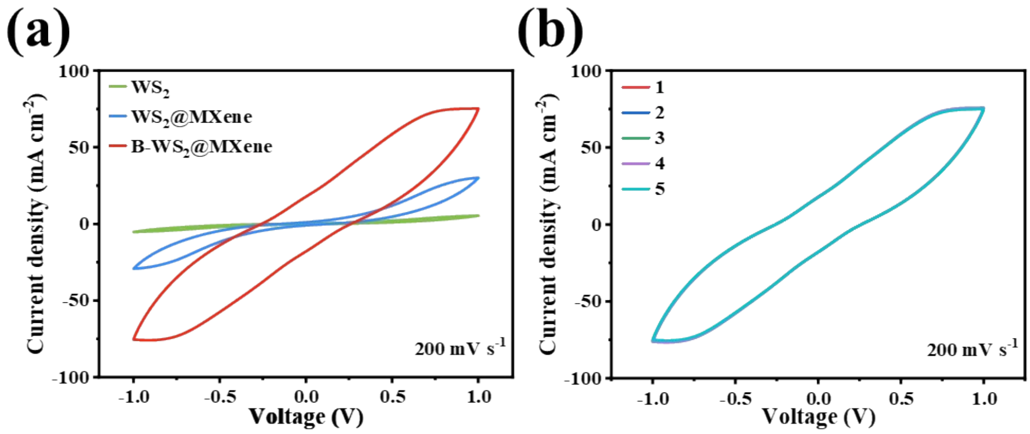

Fig. S22. CV profiles of B-WS_2@MXene for consecutive cycles.

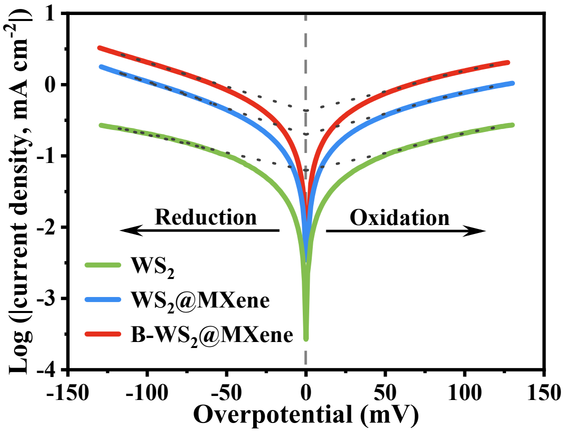

Fig. S23. Tafel plots for WS_2, WS_2@MXene and B-WS_2@MXene

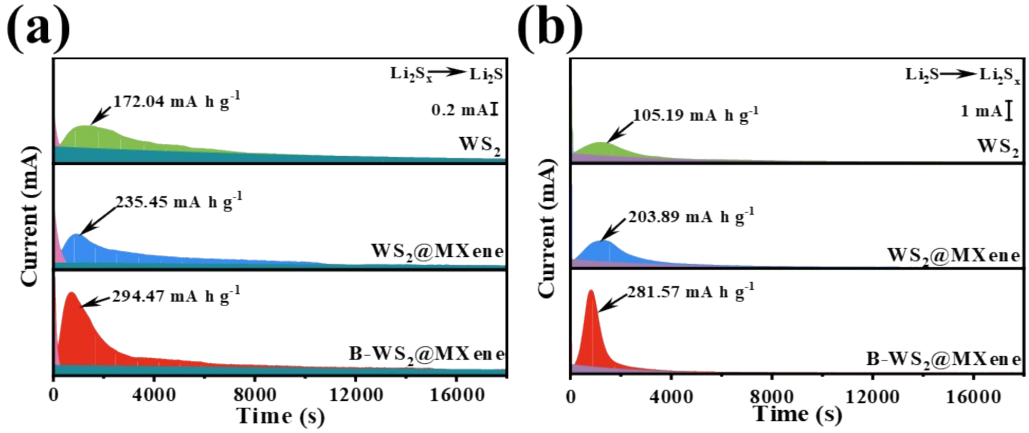

Fig. S24. (a) 2.05 V discharge and (b) 2.40 V charge potentiostatic profiles for WS_2, WS_2@MXene, and B-WS_2@MXene.

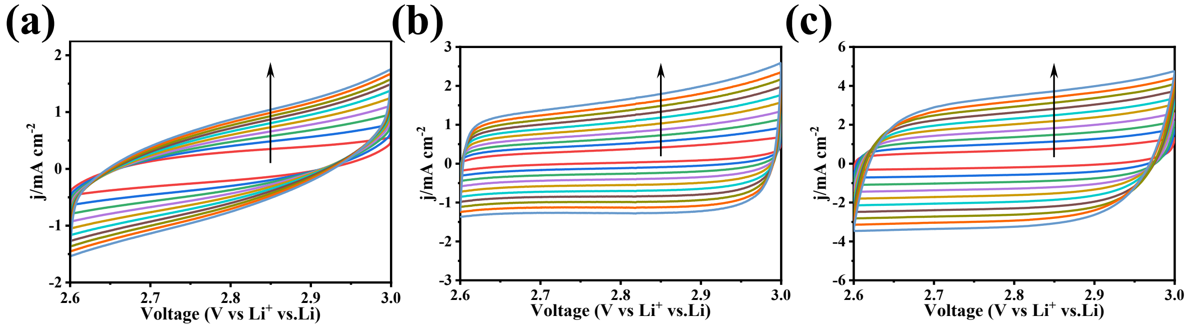

Fig. S25. CV curves in the non-faradic current range under different scan rates (10-100 mV s^{-1}). (a) WS_2. (b) WS_2@MXene. (c) B-WS_2@MXene.

Table S1. Comparison of electrochemical performance of present work with reported modified separators for carbon-based heterojunctions.

Ref.	Material	Initial capacity (mA h g^{-1})	Cycle number	Areal capacity (mA h cm^{-2})	Sulfur loading (mg cm^{-2})	E/S ratio (μL mg^{-1})
[S1]	SnSSe/rGO@PP	1521.9	1200	7	11.2	9
[S2]	Cu-N_1C_2-$Ti_3C_2T_x$-PP	1468	1000	5.28	7.19	~
[S3]	Zn-NC@MXene-PP	1135	800	5.36	3.28	~
[S4]	Fe_3Se_4/FeSe@MXene/PP	1104.5	600	~	5.8	~
[S5]	CoS_2/Fe_7S_8/NG-PP	1459	500	~	3.8	~
[S6]	MCCoS/PP	1340.7	1000	6.34	7.7	7.5
[S7]	HE-MXene/G@PP	1358.8	1200	5.71	7.8	5.6
[S8]	WP@NPC-PP	1494	1000	~	4.9	~
[S9]	CoN@NCNT	1208.4	800	~	~	~
[S10]	OMC-g-MXene@PP	1235	800	4.5	7.08	7.7
[S11]	Nb_2O_{5-x}/Ru-3DG-PP	1156.2	1000	5.6	6.3	8.9
[S12]	P-CoS_2/CNT-PP	1276.2	1000	1.75	3.6	7
[S13]	Co@NCNT-$MoSe_2$-PP	1498.5	1000	5.24	5	7.5
[S14]	Co/$Co_{0.85}$Se@NC-PP	1466	1000	10	10.7	5.8
[S15]	NbB_2/rGO-PP	1194.4	1000	4.18	7.06	8
[S16]	Co_3Fe_7-MXene-PP	1175.15	500	~	3.2	4
[S17]	$MoSe_2$-NSHC-PP	1402	800	~	3.2	6
[S18]	MoS_2-SnS/NC-PP	1504.6	400	~	3.05	8
[S19]	Ni@C/CNT-PP	1413	600	6.6	9	6
[S20]	Ni-NC-PP	1407	700	5.17	6.17	~
This work	**B-WS_2@MXene-PP**	**1593.09**	**1000**	**7.22**	**7.15**	**5**

Table S2. The mass of each component for the pouch cell.

Component	Mass (g)
Cathode	0.262
Separator	0.260
Anode	0.100
Electrolyte	0.820
Pouch	1.486
Tab & label	0.122
Total	3.050

Table S3. The volume of each component for the pouch cell.

Component	Thickness (μm)	Volume (cm^{-3})
Cathode	110	0.275
Separator	30	0.075
Anode	60	0.15
Electrolyte	~	0.083
Pouch	230	0.575
Total	430	1.075

Table S4. Parameters of the pouch cell.

Parameters	**Value**
Sulfur content	90%
Areal sulfur loading	5 mg cm^{-2}
N/P ratio	1.71
Sulfur amount	0.174 g
E/S ratio	4.8 μL mg^{-1}
Total capacity (1st cycle)	204 mA h
Areal capacity	20.7 mA h cm^{-2}
Specific energy density	140.46 W h kg^{-1}
Core energy density	297.09 W h kg^{-1}
Volumetric energy density	400.46 W h L^{-1}

Note: The ratio of E/S expresses the ratio between the volume of electrolyte and the total sulfur content and can be calculated by the following equation：

$$\frac{E}{S}=\frac{V_{\text{eletrolyte}}}{m_{\text{sulfur}}}=\frac{m_{\text{eletrolyte}}}{\rho_{\text{eletrolyte}} m_{\text{sulfur}}} \quad (8)$$

$=0.82\ \text{g}/\ (0.98\ \text{g mL}^{-1} \times 0.174\ \text{g}) = 4.8\ \mu\text{L mg}^{-1}$

N/P represents the ratio between the negative and positive capacity, which can be calculated by the following equation：

N/P = capacity of the anode/capacity of the cathode = $m_{\text{anode}} C_{\text{anode}}/\ m_{\text{cathode}} C_{\text{cathode}}$ (9)

where m_{anode} is the mass of lithium anode (g), C_{anode} is the theoretical specific capacity of lithium (mA h g^{-1}), m_{cathode} is the mass of active material sulfur (g), C_{cathode} is the discharge specific capacity (mA h g^{-1}). N/P was thus calculated as follows:

N/P = 100 mg × 3862 mA h g^{-1}/ (174 mg × 1295.6 mA h g^{-1}) =1.71

Areal capacity is defined as the ratio of the total capacity of the battery to the electrode area. The total capacity of the battery is determined by the reversible capacity of the first cycle, while the electrode area is 5cm × 5cm.

Areal capacity =204 mA h /25 cm^{-2} = 20.7 mA h cm^{-2}

The energy density per unit weight of a pouch battery can be calculated using the following equation:

$$E_g = \frac{CV}{m} \quad (10)$$

where E_g is the specific energy density (W h kg^{-1}), C is the total capacity (mA h), V represents the average output voltage (V = 2.1 V), and m is the total weight of the pouch cell, as shown in Table S2. E_g was thus calculated to be 140.46 W h kg^{-1}. Note that if do not consider the mass of the package, the core energy density E_g could reach 297.09 W h kg^{-1}.

The volumetric energy density of the pouch cell was calculated by the following equation:

$$E_{Vol} = \frac{CV}{Volume} \quad (11)$$

where E_{Vol} is the volumetric energy density (W h L^{-1}), C is the total capacity (mA h), V represents the average output voltage (V = 2.1 V), and Volume is the volume of the cell components. E_{Vol} was thus calculated to be 400.46 W h L^{-1}.

References

1. Z. Yang, Z. Guo, X. Wang, W. Lu, Q. Wang, Y. Zhao, M. Yao, P. Gao, D. Zhang and F. Du, *Energy Stor. Mater.*, 2024, **67**, 103276.
2. H. Gu, W. Yue, J. Hu, X. Niu, H. Tang, F. Qin, Y. Li, Q. Yan, X. Liu, W. Xu, Z. Sun, Q. Liu, W. Yan, L. Zheng, Y. Wang, H. Wang, X. Li, L. Zhang, G. Xia and W. Chen, *Adv. Energy Mater.*, 2023, **13**, 2204014.
3. Q. He, Z. Li, M. Wu, M. Xie, F. Bu, H. Zhang, R. Yu, L. Mai and Y. Zhao, *Adv. Mater.*, 2023, **35**, 2302418.
4. X. Zhou, Y. Cui, X. Huang, Q. Zhang, B. Wang and S. Tang, *Chem. Eng. J.*, 2023, **457**, 141139.
5. P. Chen, T. Wang, F. Tang, G. Chen and C. Wang, *Chem. Eng. J.*, 2022, **446**, 136990.
6. S. Tian, Q. Zeng, G. Liu, J. Huang, X. Sun, D. Wang, H. Yang, Z. Liu, X. Mo, Z. Wang, K. Tao and S. Peng, *Nano-Micro Lett.*, 2022, **14**, 196.
7. Q. Liang, S. Z. Wang, X. M. Lu, X. H. Jia, J. Yang, F. Liang, Q. Y. Xie, C. Yang, J. Qian, H. J. Song and R. J. Chen, *ACS Nano*, 2024, **18**, 2395-2408.
8. C. Li, J. Yu, C. Zhang, D. Yang, J. Wang, H. Li, C. Huang, K. Xiao, Y. Cheng, Y. Ren, X. Qi, T. Yang, J. Li, J. Wang, G. Henkelman, J. Arbiol, J. Nan and A. Cabot, *J. Colloid Interface Sci.*, 2024, **670**, 61-72.
9. H. Jia, J. Fan, P. Su, T. Guo and M. C. Liu, *Small*, 2024, **20**, 2311343.
10. X. Li, Q. Guan, Z. Zhuang, Y. Zhang, Y. Lin, J. Wang, C. Shen, H. Lin, Y. Wang, L. Zhan and L. Ling, *ACS Nano*, 2023, **17**, 1653-1662.
11. R. Chu, T. T. Nguyen, H. Song, Y. Bai, D. T. Tran, N. H. Kim and J. H. Lee, *Appl. Catal. B Environ.*, 2024, **352**, 124030.
12. G. Zhang, X. Chen, X. Yu, Q. Li, H. Wang, S. Hu, J. Jiang, Y. Huang and Z. Ma, *Chem. Eng. J.*, 2024, **488**, 150696.
13. X. Wang, K. Xu, J. Guo, Z. Li, S. Liu, L. Sun, J. Zhao, H. Liu, W. Liu and F. Wang, *Chem. Eng. J.*, 2024, **486**, 150301.
14. H. Xu, Q. Jiang, K. S. Hui, S. Wang, L. Liu, T. Chen, Y. Zheng, W. F. Ip, D. A. Dinh, C. Zha, Z. Lin and K. N. Hui, *ACS Nano*, 2024, **18**, 8839-8852.
15. Y. Li, Z. Wang, H. Gu, H. Jia, Z. Long and X. Yan, *ACS Nano*, 2024, **18**, 8863-8875.
16. Z. Wang, H. Jiang, C. Wei, K. Tian, Y. Li, X. Zhang, S. Xiong, C. Zhang and J. Feng, *Adv. Funct. Mater.*, 2024, **34**, 2315178.
17. Q. Sheng, H. Liu, Y. Liu, B. Jin, M. Cui, Y. Li, N. Gao, X. Lang and Q. Jiang, *Chem. Eng. J.*, 2023, **476**, 146880.
18. J. Zhang, W. Xi, F. Yu, Y. Zhang, R. Wang, Y. Gong, B. He, H. Wang and J. Jin, *Chem. Eng. J.*, 2023, **475**, 146009.
19. H. Zhang, J. Chen, Z. Li, Y. Peng, J. Xu and Y. Wang, *Adv. Funct. Mater.*, 2023, **33**, 2304433.
20. R. Wang, J. Qin, F. Pei, Z. Li, P. Xiao, Y. Huang, L. Yuan and D. Wang, *Adv. Funct. Mater.*, 2023, **33**, 2305991.